Geophysical Journal International

Geophys. J. Int. (2017) **208,** 306–320
Advance Access publication 2016 October 20
GJI Seismology

doi: 10.1093/gji/ggw393

Variability of earthquake stress drop in a subduction setting, the Hikurangi Margin, New Zealand

Rachel E. Abercrombie,[1] Stephen Bannister,[2] John Ristau[2] and Diane Doser[3]

[1]*Department of Earth and Environment, Boston University, Boston, MA* 02215, *USA. E-mail: rea@bu.edu*
[2]*GNS Science, 1 Fairway Drive, Avalon* 5010 *PO Box* 30-368, *Lower Hutt* 5040, *New Zealand*
[3]*Department of Geological Sciences, University of Texas at El Paso,* 500 *W. University Ave El Paso, TX, USA*

Accepted 2016 October 14. Received 2016 October 4; in original form 2016 May 26

SUMMARY

We calculate stress drops for 176 earthquakes (M2.6–M6.6) from four sequences of earthquakes in New Zealand. Two sequences are within the subducting Pacific plate (2014 Eketahuna and 2005 Upper Hutt), one in the over-riding plate (2013 Cook Strait) and one involved reverse faulting at the subduction interface (2015 Pongaroa). We focus on obtaining precise and accurate measurements of corner frequency and stress drop for the best-recorded earthquakes. We use an empirical Green's function (EGF) approach, and require the EGF earthquakes to be highly correlated (cross-correlation ≥ 0.8) to their respective main shocks. In order to improve the quality, we also stack the spectral ratios and source time functions obtained from the best EGF. We perform a grid search for each individual ratio, and each stacked ratio to obtain quantitative uncertainty measurements, and restrict our analysis to the well-constrained corner frequency measurements. We are able to analyse both *P* and *S* waves independently and the high correlation between these measurements strengthens the reliability of our results. We find that there is significant real variability in corner frequency, and hence stress drop, within each sequence; the range of almost 2 orders of magnitude is larger than the uncertainties. The four sequences have overlapping stress drop ranges, and the variability within a sequence is larger than any between different sequences. There is no clear systematic difference in the populations analysed here with tectonic setting. We see no dependence of the stress drop values on depth, time, or magnitude after taking the frequency bandwidth limitations into consideration. Small-scale heterogeneity must therefore exert a more primary influence on earthquake stress drop than these larger scale factors. We confirm that when fitting individual spectral ratios, a corner frequency within a factor of three of the maximum signal frequency is likely to be underestimated. Stacked ratios are smoother and more reliable near the frequency limits. We find that only corner frequencies within about a factor of two of the maximum signal frequency are likely to be underestimated.

Key words: Earthquake dynamics; Earthquake ground motions; Earthquake source observations; Seismicity and tectonics; Body waves; Subduction zone processes.

1 INTRODUCTION

The idea that the stress release (or stress drop) during an earthquake depends on its depth, tectonic setting and stress conditions has a long history, for example, Sibson (1974) and Kanamori & Anderson (1975). Global studies of earthquake sources have found that thrusting earthquakes at subduction zones appear to have systematically lower stress drops than normal faulting earthquakes within subducting slabs, strike-slip earthquakes within the oceans and intraplate earthquakes in general, for example, Choy *et al*. (2006) and Allmann & Shearer (2009). Regional studies have also reported spatial and temporal variations in stress drop. Oth (2013) found a dependence on heat flow in Japan, and Oth & Kaiser (2014) found that the intraplate earthquake sequence in Canterbury, New Zealand, had a higher median stress drop than the earthquakes in regions of Japan with higher seismicity rates. Viegas *et al*. (2010) also estimated higher stress drops for intraplate earthquakes, in eastern North America. Shearer *et al*. (2006) and Allmann & Shearer (2007) reported varying stress drop in regions of California, and Hardebeck & Aron (2009) found stress drop to depend on earthquake depth and faulting mechanism.

Understanding any dependence of earthquake stress drop on tectonic setting is not just important for determining the factors controlling dynamic rupture, but also for predicting future ground motion

and seismic hazard (e.g. Field *et al*. 2015). For example, the unexpectedly high ground accelerations and associated damage in the 2010 Christchurch earthquakes have been interpreted as resulting from higher stress drops than included in the New Zealand hazard model (Fry & Gerstenberger 2011; Holden 2011). One of the most significant sources of uncertainty in predicting high-frequency ground motions is the choice of a correct range of earthquake stress drops (e.g. Nakano *et al*. 2015).

Estimates of earthquake stress drop in many individual studies range over several orders of magnitude; it is not clear how much of this range is real variation between earthquakes and how much a consequence of the large uncertainties inherent in stress drop estimation (Cotton *et al*. 2013). This uncertainty makes it hard to confirm spatial or temporal variation in stress drop and the controversy over whether earthquakes are self-similar, with stress drop independent of seismic moment, continues. For example, Calderoni *et al*. (2013) and Pacor *et al*. (2016) both found increasing stress drop with increasing seismic moment for the 2009 Aquila earthquake sequence in Italy, whereas Shearer *et al*. (2006), Kwiatek *et al*. (2011) and Oth & Kaiser (2014) found no dependence of stress drop on moment for earthquakes in California, South Africa and New Zealand, respectively.

Improving stress drop measurement and also better quantifying the uncertainties involved are clearly necessary steps to resolve the outstanding questions concerning the controls on earthquake stress release and rupture dynamics, and the resulting seismic hazard.

An earthquake seismogram, $s(t)$, is the convolution of the radiation from the earthquake source, $e(t)$, with the combined propagation effects, $G(t)$, along the path, including both near source and site effects, and finally the instrument response, $I(t)$.

$$s(t) = e(t) * G(t) * I(t). \quad (1)$$

If $I(t)$ can assumed to be known, then the problem is to separate $e(t)$ and $G(t)$ correctly, and this is the source of much of the uncertainty in stress drop measurements. The finite, and often limited, frequency bandwidth of seismic recordings makes this separation harder. Simply modelling recorded amplitude spectra with source and attenuation models leads to large trade-offs between parameters (e.g. *Ko et al*. 2012), and underestimation of the stress drop (Kwiatek *et al*. 2014). Using a small, co-located earthquake as an empirical Green's function (EGF) to correct for all propagation effects is perhaps the simplest method of isolating the source process (e.g. Mori & Frankel 1990), but using an imperfect EGF could introduce significant uncertainty. Several approaches have been developed that make use of large numbers of earthquakes recorded at the same station group, to increase stability and obtain more reliable parameters. Oth *et al*. (2011) described a generalized inversion technique that solves for source parameters, attenuation and site effects within a large data set, which has since been applied to earthquakes in New Zealand (Oth & Kaiser 2014) and Italy (Pacor *et al*. 2016). Shearer *et al*. (2006) stacked large numbers of spectral ratios in an EGF-based approach to resolve source parameters for earthquakes in southern California. They found spatial variation, but with large variability; considering only the earthquakes with larger numbers of recordings decreased the scatter significantly. The same stacking approach has since been applied on a smaller scale to Parkfield (Allmann & Shearer 2007), Salton Sea (Chen & Shearer 2011) and Hayward (Hardebeck & Aron 2009), all in California. These approaches are likely to produce reliable average results, but the relatively large spatial averaging used in these methods may affect resolution and reliability of individual events, especially the smaller ones.

Abercrombie (2013, 2014, 2015) focused on analysing smaller numbers of well-recorded events to investigate the resolution and uncertainties of the stress drop measurements. Using the M6 Wells, Nevada, 2008 earthquake and its aftershock sequence, Abercrombie (2013) found that when an earthquake is used as the smaller in a spectral ratio, then its corner frequency (used to calculate stress drop) is likely to be underestimated compared to when it is the larger. Abercrombie suggested that this could be a consequence of the EGF assumptions as a function of frequency. For two earthquakes with collocated centroids, each point of the small earthquake source is within one fault length of the larger earthquake, but each point on the large earthquake source is not within one fault length of the small earthquake. Abercrombie (2014) compared detailed borehole EGF analysis of three repeating sequences of earthquakes at Parkfield to the same events analysed in the larger scale study of surface recordings by Allmann & Shearer (2007). She found that both studies agreed for the largest, best-recorded sequence; it is possible to calculate precise relative stress drops for well-recorded, simple earthquakes, with detailed analysis, as also observed by Uchida *et al*. (2012). The stress drops for the other two Parkfield sequences analysed by both Abercrombie (2014) and Allmann & Shearer (2007) were completely uncorrelated between the studies. The earthquakes in one sequence were probably too small and high frequency for resolution with the surface data, while the other sequence clearly involved complex ruptures not adequately modelled by the assumed simple source models. Abercrombie (2015) attempted to quantify some of the uncertainties introduced in EGF analysis by the choice of EGF, and the quality and quantity of recordings. She found that if an EGF event is more than about a source dimension distant from the larger, target earthquake, then the stress drop could be significantly underestimated. This is consistent with the EGF investigation by Kane *et al*. (2013). Prieto *et al*. (2006) and Del Gaudio *et al*. (2015) also found that using different EGFs significantly affects the results, and they favoured combining multiple EGFs for this reason. Abercrombie (2015) also demonstrated that as the corner frequency of an earthquake approaches the upper limit of the frequency bandwidth, it may be severely underestimated. Underestimation of the stress drop for the smaller earthquakes and the selection bias caused by finite bandwidth can lead to an artificial appearance of stress drop depending on seismic moment (e.g. Hardebeck & Aron 2009).

In addition to the problems outlined above, all of these approaches assume that earthquakes can be adequately modelled as simple, circular sources, with constant rupture velocity. While known differences between relatively standard models (e.g. Brune 1970; Madariaga 1976) can easily be adjusted to compare studies, Kaneko & Shearer (2015) used numerical simulation to demonstrate that, even within a range of simple rupture scenarios, significant uncertainties in stress drop are possible. This can be further exacerbated by poor azimuthal coverage.

The combination of inherent uncertainties and ambiguities, combined with different modelling approaches and data types, makes it very hard to resolve reliable variation in earthquake stress drop with tectonic setting. New Zealand is an optimal place to address this as the extreme diversity of tectonic settings in a relatively small region maximizes the chances of real variation, and consistent centralized networks provide a coherent data set of earthquakes with similar recording quality. We therefore identify four earthquake sequences from very different tectonic settings related to the Hikurangi subduction zone: the upper overlying (Australian) plate, the subducting (Pacific) plate and on the plate interface itself. These sequences are all well recorded by the regional and national networks, and we analyse them in an identical manner to determine whether there are

clear systematic differences between the earthquakes in the different settings.

We begin by describing the sequences and the data. We then apply the methods developed by Abercrombie (2013, 2014, 2015). We develop the methods further by stacking the spectral ratios, and compare results from both approaches.

2 EARTHQUAKE SEQUENCES AND DATA

We focus on four recent, earthquake sequences that occurred around southern North Island, New Zealand, in distinct tectonic environments: near Upper Hutt, Eketahuna, Cook Strait and Pongaroa (Fig. 1). The sequences are all well recorded by the GeoNet national (broadband, 100 samples s^{-1}) and regional (short period, 100 samples s^{-1}) seismometer network (Gale *et al*. 2015; see Data and Resources). We also include seismograms from the national strong motion network (50 samples s^{-1}) for the Eketahuna sequence. The station spacing (~20 km and larger) and sampling rate of these stations are best for analysing earthquakes in the M 3.5–5 range. Earthquake locations in New Zealand are routinely determined by GeoNet (www.geonet.org.nz) using the 3-D velocity model of Eberhart-Phillips *et al*. (2010). The hypocentres of the earthquake aftershock sequences discussed below were initially derived by GeoNet, and then refined for this study using double-difference relocation (Waldhauser & Ellsworth 2000), both with waveform-based differential times calculated for all event-station pairs using ObsPy (Beyreuther *et al*. 2010). All hypocentres are provided in Table S1 (Supporting Information).

2.1 Upper Hutt: normal faulting within subducting slab

In 2004, an earthquake sequence began in the subducted Pacific plate in the southern Hikurangi subduction zone (Fig. 1), likely triggered by slow slip at the plate interface (Reyners & Bannister 2007). The largest earthquakes in the sequence had normal-faulting mechanisms, and were precisely relocated by Reyners & Bannister (2007) to lie within the crust of the subducting plate. The largest earthquake occurred in 2005 January (M_L 5.5), and it is this earthquake, and its aftershock sequence that we analyse here. This sequence, below Upper Hutt in the Wellington region, was well recorded by the regional and national seismometer networks. It was a relatively small sequence, but we select it for analysis because of its similarity in tectonic setting to the 2014 Eketahuna sequence.

2.2 Eketahuna: normal faulting within subducting slab

In 2014 January, an M_L 6.2 earthquake occurred in the subducted Pacific plate beneath Eketahuna, with shaking felt throughout New Zealand. It was also a normal faulting event, and was likely associated with deeper slow slip on the subduction interface (Wallace *et al*. 2014). The Eketahuna earthquake was followed by a well-recorded extensive aftershock sequence within the thickened crust (Davy *et al*. 2008) of the subducting plate, and we analyse these earthquakes here.

2.3 Cook Strait: strike-slip faulting in upper plate

On 2013 July 21, an M_w 6.6 earthquake occurred within the overlying crust in Cook Strait, causing widespread shaking in the Wellington and Marlborough regions (Holden *et al*. 2013). The earthquake involved a pure right-lateral rupture at about 16 km depth and was followed by a strong, well-recorded aftershock sequence. The event was followed in August by the M_w 6.6 Grassmere earthquake and corresponding aftershock sequence, ~25 km to the south. Hamling *et al*. (2014) modelled the geodetic data from the Cook Strait July earthquake to estimate a rupture length of 25 km and a slip of 90 cm. They concluded that the event was triggered by the largest two foreshocks (M_w 5.7 and M_w 5.8), and that, in turn, triggered the subsequent Grassmere earthquake.

2.4 Pongaroa: thrust faulting on plate interface

The Pongaroa earthquake (M_w 5.7) and aftershocks (between M_L 4.4 and M_L 1.4) occurred in 2015 November. The depth and the moment tensor of the main shock (http://www.geonet.org.nz; last accessed: 2016 May 26) are consistent with reverse faulting on the subduction interface.

3 EMPIRICAL GREEN'S FUNCTION ANALYSIS

We begin by selecting potential EGFs and seismogram time windows. We then use the cross-correlation between the EGF and target event (or main shock) seismograms to identify the best EGFs for spectral analysis. We follow the analysis procedure of Abercrombie (2014) and Viegas *et al*. (2010) to calculate corner frequency. We use both *P* and *S* waves, on all three components.

3.1 Seismogram and EGF selection

For each sequence, we start with the largest earthquake as the target event, and work down in magnitude until the earthquakes are too small to resolve source parameters within the frequency range of the available data. The earthquakes and stations are shown in Fig. 1. Table S1 (Supporting Information) lists the hypocentres of the earthquakes studied. For each target earthquake in turn, we identify potential EGF events from the catalogues, following the approach of Abercrombie (2013, 2014, 2015). We start by using relatively broad distance and magnitude-based criteria to compensate for location uncertainties. We include all earthquakes within 2 km epicentral distance of the target earthquake, and between 1 and 2.5 mag units smaller. This distance is significantly larger than the likely source dimension of most of these earthquakes. We do not use the depth as a constraint as the depth uncertainties are larger. We use a larger (10 km) radius for the largest target earthquakes ($M_L \geq 5.5$) because they have larger source dimensions. We then use waveform cross-correlation to select good EGF events for further analysis.

As we are using a wide magnitude range of earthquakes, we choose a time window for analysis based on the magnitude of the target earthquake. Previous work has found that a time window of 0.5–1 s is good for an M1–2 (e.g. Abercrombie 1995; Ide *et al*. 2003; Shearer *et al*. 2006). Using this window, and assuming constant (low) stress drop scaling (stress drop ~0.1 MPa, *S* velocity ~4 km s^{-1}), we can calculate a window length (*nsec*) that is of the order of 10 times the expected pulse duration of the target earthquake using:

$$nsec = \text{round}\left(10 \times M_0^{1/3}/20000\right)/10 \quad (2)$$

where M_0 is the seismic moment of the target earthquake. If the window length is greater than 30 s (equivalent to M_w 5.5), then it is

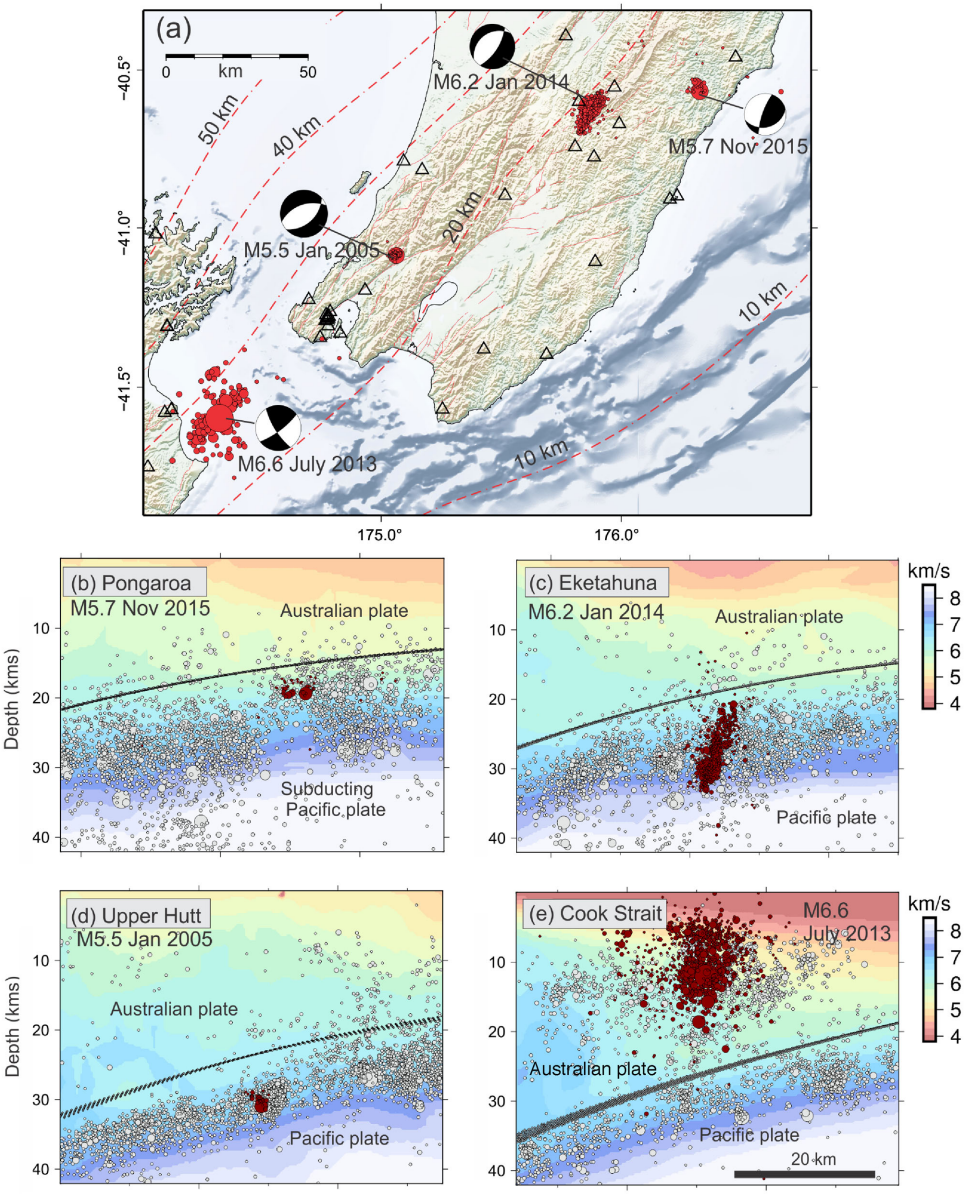

Figure 1. (a) Epicentres of the four earthquake sequences, lower North Island, New Zealand (red circles), as detailed in Table S1 (Supporting Information). The main shock focal mechanisms shown for each sequence were derived by moment tensor inversion (http://www.geonet.org.nz; last accessed: 2016 May 26), plotted with upper hemisphere projection. GeoNet seismometer site locations are shown as open triangles. Contours with dashed red lines show the depth to the subduction interface, as derived by Williams *et al*. 2013. (b)–(e) NW-SE cross-sections of each of the four earthquake sequences. White open circles show background seismicity for years 2001–2011 for earthquakes within 40 km of each cross-section; red circles show the projection of the aftershock sequence hypocentres. The grey line shows the depth of the subduction interface estimated by Williams *et al*. (2013). *P* wave (km s^{-1}) is shown in the background, from the 3-D New Zealand velocity model of Eberhart-Phillips *et al*. (2010).

set to 30 s. We do this as we do not consider any earthquakes with an expected source duration more than 30/2 s, and because using much longer windows prevents the use of *P* waves for local recordings of the larger earthquakes. Using a moment-dependent window length increases the number of local *P*-wave recordings that can be used for the smaller earthquakes.

We then consider each target earthquake in turn, using the same value of *nsec* for the target earthquake and all EGFs. To calculate the cross-correlation between seismograms, we bandpass filter to an appropriate frequency band, using a two-pole Butterworth filter. We low-pass filter both the target earthquake and each potential EGF at a frequency related to the expected corner frequency of the target event, assuming constant stress drop. This is because large and small earthquakes are not expected to cross-correlate well at high frequencies (e.g. Abercrombie 2015).

$$lowpassf = 10/nsec. \tag{3}$$

We use a default high-pass corner of 0.5 Hz to remove microseismic noise (large in New Zealand), decreasing it to *lowpassf*/5 for the largest earthquakes ($M > 5.5$) when the *lowpassf* approaches 0.5 Hz. We then calculate the cross-correlation between the filtered target earthquake and the EGF seismograms, within the selected time windows, treating *P* and *S* waves individually. We discard all seismogram pairs (per EGF, per station, per component) where

the cross-correlation is <0.7. Abercrombie (2015) found that using EGFs with such low cross-correlations significantly biases the source parameter results.

If the pair of seismograms (target and EGF) has a cross-correlation of ≥0.7, we calculate their spectra and spectral ratios using the multitaper method of Prieto *et al*. (2009) and the unfiltered seismograms. This approach produces the most reliable amplitude spectra (e.g. Park *et al*. 1987; Prieto *et al*. 2009), and the complex division enables us to extract the relative source time function (STF) of the target earthquake from each ratio. Deconvolution of a clear source pulse confirms the EGF assumptions, since the approximation is good enough to work in phase as well as amplitude. Observation of the STF also assists in identifying complex sources that are not well fit by the simple source models (e.g. Abercrombie 2014). Two examples are shown in Fig. 2 and more in Fig. S1 (Supporting Information).

3.2 Individual ratio fitting for corner frequency

We follow the approach of Abercrombie (2014), and fit each individual spectral ratio (of target event to EGF) to calculate the corner frequencies using the spectral source model (Brune 1970; Boatwright 1980):

$$\frac{\dot{M}_1(f)}{\dot{M}_2(f)} = \frac{M_{01}}{M_{02}} \left(\frac{1 + \left(f/f_{c1}\right)^{\gamma n}}{1 + \left(f/f_{c2}\right)^{\gamma n}} \right)^{\frac{1}{\gamma}} \tag{4}$$

where f is frequency, f_{c1} and f_{c2} are the corner frequencies of the large and small earthquakes (target and EGF), respectively, M_{01} and M_{02} are the seismic moments of the large and small earthquakes, respectively, n is the high-frequency fall-off (we assume $n = 2$) and γ is a constant controlling the shape of the corner. We try both the original Brune (1970) model ($\gamma = 1$), and the sharper-cornered Boatwright (1980) model ($\gamma = 2$). The sharper-cornered model gave a better fit overall to the majority of the spectral ratios, with a systematically lower variance of fit between the model and observed spectral ratios. This was also true for the stacked ratios considered later, and for earthquakes analysed using the same methods from Nevada (Ruhl *et al*. 2016). We use this sharper-cornered model in all subsequent analysis.

Before fitting, we log sample the spectral ratios in frequency to decrease the weighting towards the higher frequency part of the spectra. The samples are defined at intervals of Δf where $\log_{10}(\Delta f) = 0.05$, between $1/nsec$ and 200 Hz (above the Nyquist frequency of the highest sampling rate data) to enable comparison and stacking of the spectral ratios from stations with different sample rates. (All EGFs for a target earthquake have the same value of *nsec* as the target earthquake.) For each spectral ratio, we use only the frequency range in which (at each sample) the signal of both large and small events is at least three times the spectral amplitude level in a noise window immediately preceding, and of the same length as, the respective signal window. The noise windows for the *S* waves include the *P*-wave coda, and so there is no danger of contamination of the *S* spectra with *P*-wave energy at higher frequencies. We fit the individual spectral ratios using the Nelder–Meade inversion in MATLAB (Abercrombie & Rice 2005). Following Viegas *et al*. (2010), we perform a grid search around the resulting value of f_{c1}, to determine the range of f_{c1} and f_{c2} in which the variance of the fit of the model to the observed spectral ratio is within 5 per cent of the minimum value. We do not use the estimates of f_{c2}. They are typically out of the available bandwidth, and the results of Abercrombie (2013) suggest that they are not directly comparable with f_{c1}. Examples of the analysis are shown in Figs S2–S7 (Supporting Information).

We then use the individual measurements to calculate mean values for each target earthquake using each EGF, and for all measurements for each target earthquake. We use further selection criteria to obtain the best results, and ensure that we only include model fits

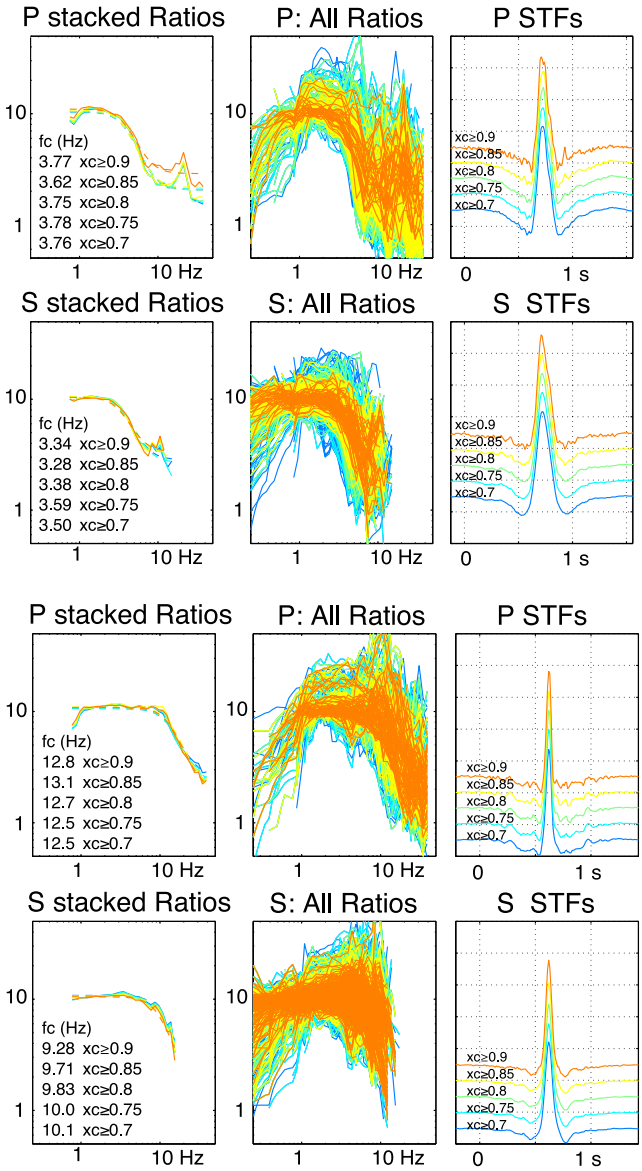

Figure 2. Spectral ratios and source time functions for two well-recorded earthquakes in the Eketahuna aftershock sequence. (a) Example of a low stress drop, well-recorded event ID468, M3.8. Top row is *P* waves and bottom row, *S* waves. LH column: stacks and fits for ratios at all EGFs and stations that have cross-correlation (xc) ≥ 0.7 (blue), to ≥0.9 (orange) and ≥0.8 (green). The numbers are the best-fitting corner frequencies, starting at bottom with xc 0.7, and going up to 0.9. Middle column: all the ratios used in the stacks, coloured in the same manner. RH column: stacked STFs, coloured in the same manner, xscale in samples at 100 s^{-1}. (b) Same as (a) but for a similar magnitude, higher stress drop event (ID327, M3.8). Note that the relocated epicentres of these earthquakes are 4 km apart, and both at 29 km; both earthquakes have similar long-period amplitudes.

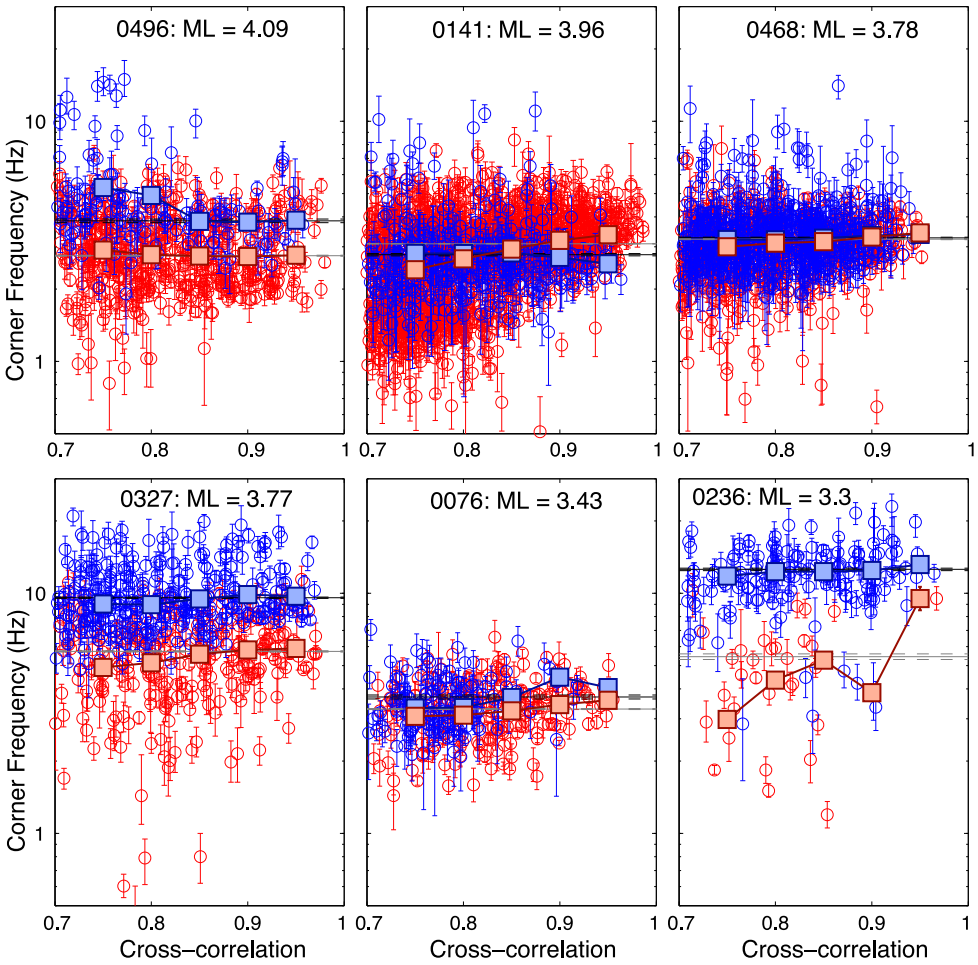

Figure 3. Corner frequency measurements on individual ratios. Results for six example target earthquakes, chosen from the Eketahuna sequence, both *P* waves (blue) and *S* waves (red). Each panel is for a single target earthquake, and each measurement is for a single ratio, with fitting errors (≤5 per cent variance increase). Mean values for the measurements with cross-correlation ≥0.8 are shown for *P* waves (black, 1 standard deviation dashed), and *S* waves (grey). The large blue and red squares are the variance-weighted means for cross-correlation bands of 0.1, plotted at their centres. The standard deviations are also shown, but most are smaller than the symbol size.

to spectral ratios with a clearly defined corner frequency. Following Viegas *et al*. (2010) and Abercrombie (2013, 2014), we require the variance to have a parabola shape with a clear minimum (variance ≤ 0.005) at the preferred corner frequency. We set the limit in the corner frequency uncertainty such that the large earthquake corner frequency variance increases by 5 per cent within a factor of two of the corner frequency measurement ($(f_{c1}\max - f_{c1}\min)/f_{c1} =$ fc1_err ≤ 2). As we do not use f_{c2}, we do not impose any limits on its uncertainty. To limit the effect of bumps and irregularity in the spectral ratios, we use only measurements where the difference in amplitude of high- and low-frequency levels in the fit is greater than 2 (fit_amp_ratio ≥ 2). These are the same limits used by Abercrombie (2014); they represent a balance between excluding all poorly resolved spectral ratios and corner frequencies, while retaining sufficient quantity of observations to obtain a reliable average, preferably with a wide azimuthal range. Examples of the results are shown in Fig. 3. There is large variability in the individual measurements demonstrating the problems of making precise corner frequency measurements for earthquakes recorded by few stations, or with few EGFs.

To ensure that the mean is not badly influenced by the poorer quality measurements included, we calculate the weighted mean ($\hat{y}$) of the corner frequency, using inverse-variance weighting which downweights values with the largest uncertainties (e.g. Hartung *et al*. 2008)

$$\hat{y} = \frac{\sum_i \left(y_i/{\sigma_i}^2\right)}{\sum_i \left(1/{\sigma_i}^2\right)}, \quad D^2\left(\hat{y}\right) = \frac{1}{\sum_i \left(1/{\sigma_i}^2\right)} \tag{5}$$

where y_i is the ith measurement, σ_i is its variance and D is the standard deviation of the weighted mean. This approach, again the same as that used by Abercrombie (2014), incorporates individual measurement uncertainties into the uncertainty of the mean and decreases the dependence of the results on the values of the selection criteria. We calculate the weighted mean for each earthquake using all available stations, components and EGFs.

To investigate further whether higher cross-correlation constraints affect the value and precision of the corner frequency measurements, we calculate the variance-weighted means within a range of cross-correlation bands (Fig. 3). Many events show a slight increase in corner frequency with cross-correlation as previously observed by Abercrombie (2015). The standard deviation decreases with increasing cross-correlation threshold in the lower bands, which have more measurements. As the cross-correlation

threshold increases, the smaller number of measurements causes the standard deviation to increase slightly.

For the Eketahuna sequence we start with 674 earthquakes $M_L \geq 2$, and for these are able to calculate source parameters for 46 of the 50 earthquakes with $M_L \geq 3.2$. For the Upper Hutt sequence, we start with 381 earthquakes $M_L \geq 2.0$, and are able to calculate source parameters for 16 of the 18 earthquakes $M_L \geq 3.0$. For the Cook Strait sequence, we start with 1125 earthquakes $M_L \geq 2$, and are able to calculate source parameters for 98 of the 291 earthquakes $M_L \geq 3.2$. Lastly, for the Pongaroa sequence, we start with 88 earthquakes $M_L \geq 1.4$, and are able to calculate source parameters for 16 of the 19 earthquakes $M_L \geq 2.6$.

3.3 Stacking spectral ratios for corner frequency

Stacking large numbers of seismograms or spectra is an efficient way of increasing the signal and cancelling out variability arising from noise. The large number of available EGFs and stations, and the large scatter in the results (Fig. 3) suggest that stacking the spectral ratios and STFs calculated here could lead to improved stability and resolution of the corner frequencies. Stacking poorer quality data, and ratios with less appropriate EGFs can potentially increase the uncertainty and bias the results (e.g. Kane *et al*. 2013; Abercrombie 2015). To minimize these problems, we investigate the effects of EGF selection by limiting the EGFs included in the stacks depending on their cross-correlation. We use minimum cross-correlation values of 0.7, 0.75, 0.8, 0.85 and 0.9. For each main event, we normalize and stack all the ratios that meet the cross-correlation threshold, from all stations and EGFs. At each frequency sample, a spectral ratio is only included in the stack if it meets the signal-to-noise criteria used for the individual fitting; the mean of the values at each frequency is only included if there are five or more samples at that frequency, see Fig. 2 and Fig. S1 (Supporting Information). As all spectra and ratios are sampled at the same logarithmically distributed frequencies, data from different sample rates can be included in the stacked spectral ratios. In order to stack the STFs we interpolate all lower sample rate data (50 samples s^{-1}) to 100 samples s^{-1}. In this study, these STFs are used simply to check the EGF procedure is working well and no measurements are made on them.

We then fit the stacked ratios using the same approach as for the individual spectral ratios, including performing a grid search to determine the uncertainties in the model fits to the ratios with varying corner frequency. We use the same quality criteria for resolvable corner frequency of the stacked spectral ratios as for the individual. A minimum frequency bandwidth of a factor of five in frequency is also imposed. By stacking over all stations, we average out any azimuthal variation but we were already doing this to calculate the average values from the individual fitting. Stacking per station to investigate whether azimuthal variation can provide more detailed source information for the best-recorded events will be attempted in a future study. Stacking over EGFs is a less common procedure. In doing so, all information about the individual EGFs is lost, but the corner frequency of the large event is preserved in all ratios and so can be calculated from the stacked spectral ratios (e.g. Uchide & Imanishi 2016).

The corner frequencies of the *P* and *S* calculated from the stacked ratios are compared in Fig. 4(a). These two corner frequencies are independent measurements and so the strong correlation between them provides evidence of the reliability of the results.

4 CALCULATION OF MOMENT AND STRESS DROP

To calculate the stress drop, we need a measure of both the finite dimension of the earthquake (here we use the corner frequency), and the seismic moment. We also need a source model to combine them, and we use the ratio of *P* and *S* corner frequencies that we calculate to select the most appropriate simple source model.

4.1 Seismic moment

The EGF approach does not calculate absolute moment, and so we need an independent measurement. For some of the larger earthquakes, we can calculate regional moment tensors (Ristau 2013), but for others we use M_w–M_L relationships to calculate M_w and hence seismic moment (Hanks & Kanamori 1979) from M_L.

We are able to calculate moment tensors for 33 earthquakes in the Cook Strait sequence, following Ristau (2013), and we use these moment values in our analysis. These regional moment tensor values are accurate to within a factor of ~1.5, from comparison with other moment catalogues (Ristau 2013). Using these moments, we calculate the relationship between M_w and M_L for the Cook Strait aftershock sequence, excluding the M6.7 main shock, and obtain $M_L = 0.7081\ M_w + 1.0267$, with uncertainties of ~0.2 M_L.

For the earthquakes beneath Upper Hutt in 2005, we calculate seismic moment from M_L, using the relationship for New Zealand from Ristau (2013): $M_L = 0.93\ M_w + 0.54$. This is consistent with the M_w 5.3 and M_L 5.5 of the largest earthquake in the sequence.

For the 2015 Pongaroa sequence, we use the updated version of M_w–M_L for New Zealand, developed following a change in the way catalogue magnitudes are calculated, in 2012: $M_L = 1.0231\ M_w + 0.0494$.

We start with this same relationship for the Eketahuna sequence but find that it systematically overestimates the seismic moment. None of the aftershocks at Eketahuna have sufficient long-period signal to calculate a moment tensor. We can just consider the long-period amplitude without inverting for moment tensor, and we do this to estimate the moment for two earthquakes (ID438 and ID496). We obtain M_w 4.3 (M_L 4.8) and M_w 3.9 (M_L 4.5), respectively. Hence, we adjust the New Zealand relationship to $M_L = 1.0231\ M_w + 0.45$ to calculate seismic moment for the Eketahuna earthquakes.

The uncertainties in the M_L measurements, their variation with respect to the seismic moments (Ristau 2013), and the (smaller) uncertainties in the regional moment tensors (Ristau 2009) combine to give an uncertainty of about a factor of 2–3 in the seismic moments estimated from M_L. The moments of the earthquakes in one sequence could be systematically overestimated or underestimated by a similar amount with respect to the other sequences.

4.2 Source model and stress drop

To calculate the stress drop ($\Delta\sigma$) from the moment and corner frequency measurements, we need a way of relating the corner frequency to source dimension, and an expression for the average slip distribution on the rupture. We assume a simple circular model and follow Eshelby (1957) to obtain

$$\Delta\sigma = \frac{7M_0}{16}\frac{f_c^3}{k^3\beta^3} \tag{6}$$

where β is the *S*-wave velocity, and k is determined by the source model. We use appropriate values for β from the New Zealand

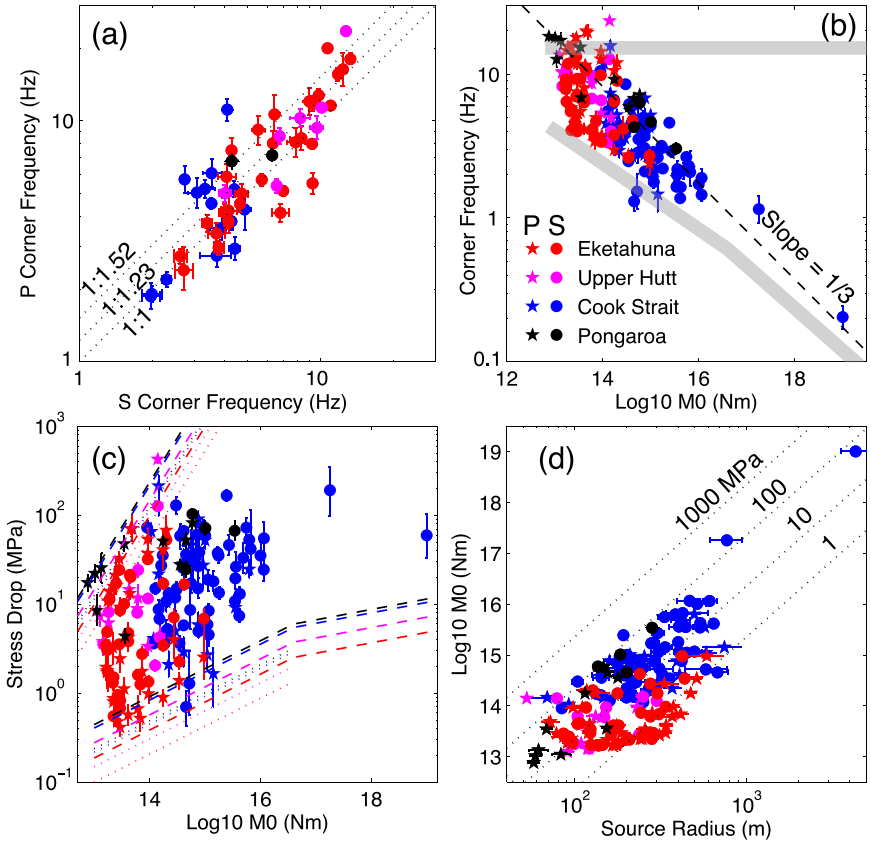

Figure 4. Source parameter results from measurements on *P*- and *S*-wave stacks of all ratios with cross-correlation of 0.8 or more. (a) Comparison of *P* and *S* corner frequencies. The dashed lines indicate fc $P = 1 \times f_cS$, $1.23 \times f_cS$ (Kaneko & Shearer 2015, model used here), and $1.52 \times f_cS$ (Madariaga 1976). (b) Corner frequency and seismic moment. The thick grey lines indicate the average limits of corner frequency resolution based on the observed signal frequency range: 15 Hz, and average minimum frequency ×2. (c) Stress drop and seismic moment. The dashed lines indicate how the results are bounded by the signal frequency bandwidth—they are the stress drops that would be obtained using corner frequencies at the limits shown in (b). The long dashes are for *S* waves and the short are for *P* waves, colours match those used to plot the values. (d) Results showing lines of constant stress drop.

3-D velocity model (Eberhart-Phillips *et al*. 2010): 4.4 km s^{-1} for Eketahuna (30 km depth), 3.86 km s^{-1} for Upper Hutt (30 km depth), 3.3 km s^{-1} for Pongaroa (18 km depth) and 3.4 km s^{-1} for Cook Strait (15 km depth). These values do not vary significantly in the source regions of the sequences; the largest variation is an increase in velocity of less than 10 per cent throughout the depth range of the crustal sequence under Cook Strait).

For the commonly used source model of Madariaga (1976), $k = 0.32$ for *P* waves and $k = 0.21$ for *S* waves, averaged over azimuth. The mean value of f_cP/f_cS for our results is ∼1.2, significantly smaller than the ratio found by Madariaga (1976). Kaneko & Shearer (2014, 2015) performed dynamic modelling of simple sources and, like Madariaga (1976), found considerable variation in k with azimuth. For a simple symmetrical circular crack model with a rupture velocity of 0.9β, they obtained similar results to Madariaga (1976). Here, we assume the values obtained by Kaneko & Shearer (2015) for a symmetrical circular model with a rupture velocity of 0.7β. This model has a $k = 0.32$ for *P* waves, the same as in the Madariaga (1976) model used by previous *P* wave only studies (e.g. Shearer *et al*. 2006; Allmann & Shearer 2007; Abercrombie 2013, 2014, 2015). For *S* waves, $k = 0.26$, which is higher than in the Madariaga (1976) model but fits the average ratio of 1.2 that we observe. We prefer this model as it makes *P* and *S* waves comparable in our data sets. Converting to other source models simply involves multiplication of the stress drop by a scalar, for example, Abercrombie & Rice (2005).

5 RESULTS AND DISCUSSION OF UNCERTAINTIES

We plot the resulting corner frequency and stress drop measurements for all the earthquakes studied in Figs 3–5. We find that despite tight constraints on both the data quality and the appropriateness of assumptions, there is still considerable scatter and variability in the results. We discuss this below before attempting to interpret the measurements themselves. Our principal conclusion is that the variability within each individual sequence is significantly larger than any systematic differences between sequences, despite the different tectonic settings. We observe no systematic trends with depth that cannot be explained by velocity differences. We find that measurement uncertainties increase as the real corner frequency approaches the high-frequency limit of the data. We also find that corner frequency measurements on stacked spectra are less affected by limited frequency bandwidth than the averaged values from fitting individual spectral ratios.

5.1 Uncertainty from cross-correlation limit

Abercrombie (2015) found a strong correlation between the stress drop obtained from EGF analysis, and the cross-correlation between the EGF and the main shock. She interpreted this as due to the appropriateness of the EGF assumption decreasing towards the shorter wavelengths needed to resolve small source dimensions and high

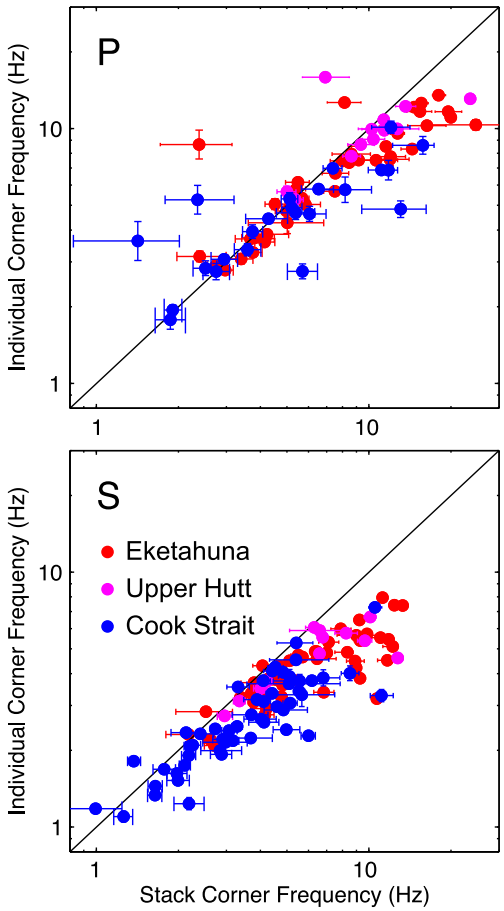

Figure 5. Comparison of corner frequency measurements made on individual ratios, and on stacked ratios, using the sharper-cornered Boatwright model. In both cases, only ratios with a minimum cross-correlation of 0.8 are included. Note that the means of the individual measurements become systematically lower than the measurements on the stacks as the corner frequency increases.

stress drops. Here, we further investigate the cross-correlation as a proxy for the appropriateness of the EGF assumption. In this study, we did not use any ratio where the cross-correlation was less than 0.7, and all EGFs were located within 2 km of the target event. We performed all the analyses using spectral ratios from pairs of seismograms with cross-correlations of at least 0.7, 0.75, 0.8, 0.85 and 0.9. The decrease in variability and improvements in the individual ratios as the minimum cross-correlation increases can be seen in Figs 2 and 3 and more examples are shown in Fig. S1 (Supporting Information). As the minimum cross-correlation limit is increased, the quantity of spectral ratios and measurements to be stacked (or averaged) decreases, limiting the advantages of stacking.

We do not observe any systematic variation in corner frequency with cross-correlation among these data, as shown in Fig. S8 (Supporting Information). Perhaps this is because we do not consider such low cross-correlations and poor-quality EGFs as Abercrombie (2015). Also, Abercrombie used repeating earthquakes with very similar corner frequencies recorded on borehole stations with very consistent signal frequency bandwidth. In this study, variation from event to event of both the corner frequency and its relationship to the actual frequency bandwidth available would potentially obscure any trends. Fig. S8 (Supporting Information) shows that the relative values of stress drop remain consistent regardless of wave type, cross-correlation threshold, or source model assumed.

We do not observe any dependence of cross-correlation and separation distance from the relocations for the best-quality spectral ratios, but this most likely reflects location uncertainty and also the effects of any variation in the focal mechanisms of the main and candidate EGF events. Using only highly cross-correlated pairs should eliminate EGFs with significantly different focal mechanisms.

For the present data, we select a minimum cross-correlation of 0.8 as being the maximum threshold value for which there is sufficient data quantity to produce stable results. This is the value we use in all subsequent discussion, but using other values does not affect the overall conclusions.

5.2 Uncertainty in calculating corner frequency: the effects of finite bandwidth, individual and stacking approaches, and spectral model shape

The finite bandwidth of seismogram signals is probably the most limiting factor in studying earthquakes over a range of magnitudes. Earthquakes with corner frequencies near the centre of the signal frequency range (bandwidth) will be the best resolved. Those with corner frequencies at or outside the signal bandwidth will often be removed during analysis because the spectral ratios cannot constrain a corner-frequency value. This leads to a strong selection bias; small earthquakes with corner frequencies above the maximum signal frequency, and large earthquakes with corner frequencies below the minimum signal frequency will simply be excluded from analysis (see Fig. 4c). Earthquakes with corner frequencies near, or above the maximum signal frequency are often pinned at the maximum value in large-scale studies (e.g. Shearer *et al*. 2006; Hardebeck & Aron 2009). In the present analysis, poorly resolved corner frequency measurements with no clear minima in the fitting variance are excluded, and so earthquakes with corner frequencies near the bandwidth limits are selectively removed. The finite signal frequency range is indicated in Figs 4(b) and (c).

In addition to this selection bias, the finite signal bandwidth can also affect measurements of corner frequency that lie within it. Modelling individual spectral ratios that meet strict quality criteria should result in high-quality results, but Figs 2 and Fig. S1 (Supporting Information) show that even then there is large variability. This is probably because of the uncertainties inherent in working with frequency band-limited data, and imperfections in the EGF correction for path effects. To attempt to decrease the variability and uncertainties, we try stacking the best spectral ratios. Unlike previous studies (e.g. Shearer *et al*. 2006), we do not simply stack the ratios of the nearest N earthquakes (where N is typically 200 events, and can represent a very broad area compared to the source dimensions of the earthquakes involved). Instead, we stack only those ratios that meet the same epicentral separation and cross-correlation criteria as considered before. We do not require each individual ratio in the stack to meet any fit_amp_ratio or fc1_err limits to include it in the stack, and so can include more spectral ratios than when fitting individually. Fig. 2 and Fig. S1 (Supporting Information) show that the stacking works well and minimizes variability in the spectral ratios.

Fig. 5 compares the corner frequencies obtained per main shock using the stacked and the individual ratio fitting methods. The inverse-variance weighting used to propagate the uncertainty in fitting the individual ratios, leads to significantly smaller formal

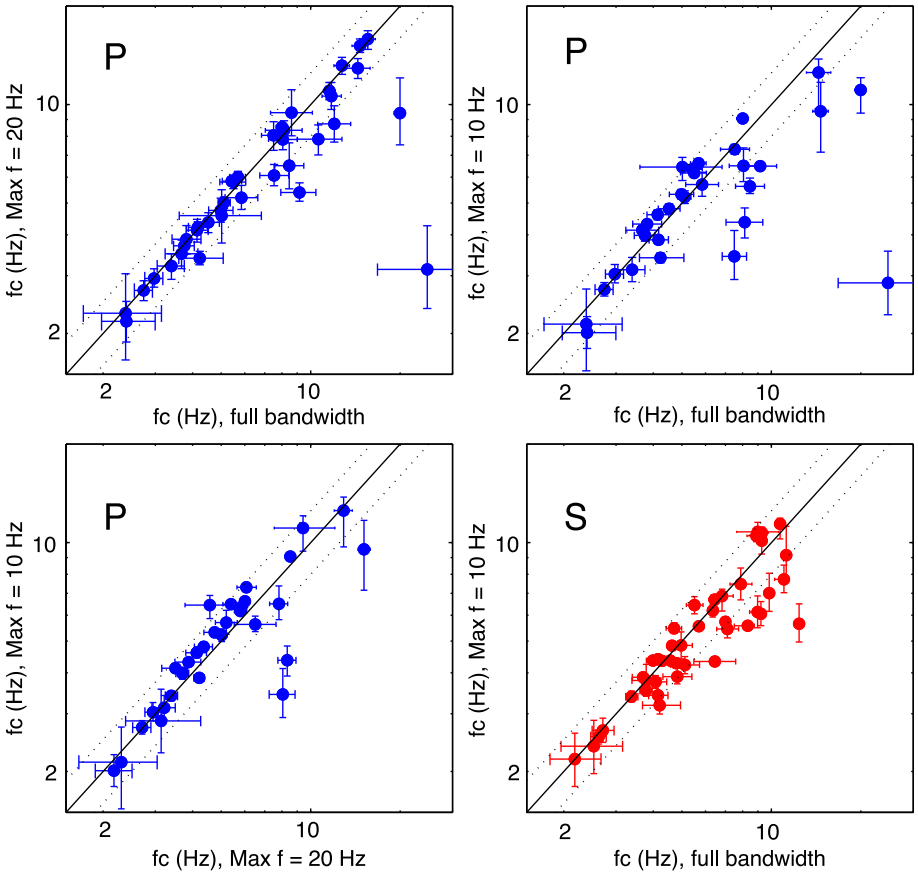

Figure 6. Effect of limited bandwidth on fitting the stacked ratios within the Eketahuna sequence. Only ratios with a minimum cross-correlation of 0.8 are included. Solid black lines indicate $x = y$, and the dashed lines are at ±25 per cent. Blue symbols are *P*-wave measurements, and red are *S*-wave measurements. In all cases, the most limited bandwidth measurements are plotted on the *y*-axis.

uncertainties in the average as the number of measurements increases. This decrease in formal uncertainty with larger number of data is not so strong for fitting the stacked spectra, and so the relative size of the error bars is not a good indication of the superiority of either method. At relatively low corner frequency, the results are similar, but at higher corner frequency the averages of the individual fits progressively underestimate the corner frequency compared to fitting the stacked ratios. Abercrombie (2015) found that corner frequencies are underestimated when they are above one-third of the maximum frequency of the signal. This would correspond to ∼12 Hz for *P* waves (typical maximum *f* 35–40 Hz), and ∼5 Hz for *S* waves (typical maximum *f* 12–16 Hz) in the present study. If anything these are optimistic limits for the present study, even assuming that the fits to the stacked ratios are unaffected by the finite bandwidth. The most likely reason for this is that as the real corner frequency increases, individual ratios with lower than average values will be well constrained, but those with higher than average corner frequency will be approaching flat lines, and the calculated corner frequencies will be unconstrained and so excluded. The result will be a tendency to bias the average to lower values. The stacked spectra include these ratios and so will be less biased; the stacked ratios are also smoother, and so corner frequencies nearer bandwidth limits can be resolved.

To investigate whether there are also systematic biases in the results from the stacked ratios, we repeat the spectral fitting of the stacked ratios, while progressively limiting their frequency range. Fig. 6 shows the effects of limiting the maximum frequency to 10 and 20 Hz for *P* and 10 Hz for *S* waves. There is a clear increase in variability at higher frequencies, and a tendency to underestimate the corner frequency as it nears the maximum value of the signal, but it is much weaker than for the individual fitting.

We conclude that by fitting stacked, carefully selected spectral ratios we should be able to resolve corner frequencies to about 50–75 per cent of the maximum frequency limit of the data (∼20 Hz for *P* waves and ∼8 Hz for *S* waves). To investigate this further, we divide the points into those with corner frequencies above and below 5 Hz. Limiting the frequency bandwidth to 20 Hz for *P* waves and 10 Hz for *S* waves results in an average underestimate for the higher corner frequency group by about 10 per cent, with a doubling of the standard deviation compared to the full-bandwidth measurements.

It is likely that similar systematic bias occurs as the corner frequency approaches the lower frequency limit of the data, but this issue affects few events in our data set and so is hard to quantify. It is mainly an issue for the largest earthquakes in a data set. Using a magnitude-dependent time window ensures that lower frequencies are included in the spectral ratios of the larger earthquakes. Unfortunately, the EGFs of the largest earthquakes have a smaller average magnitude with respect to the target event, than the majority of aftershocks. The relatively small EGF magnitudes mean that many spectral ratios lack signal at the lower frequencies needed to resolve the corner frequency of the largest earthquakes. This is a consequence of the empirical Båth's Law, and Gutenberg–Richter relations (e.g. Felzer *et al*. 2002) that mean the largest earthquakes in

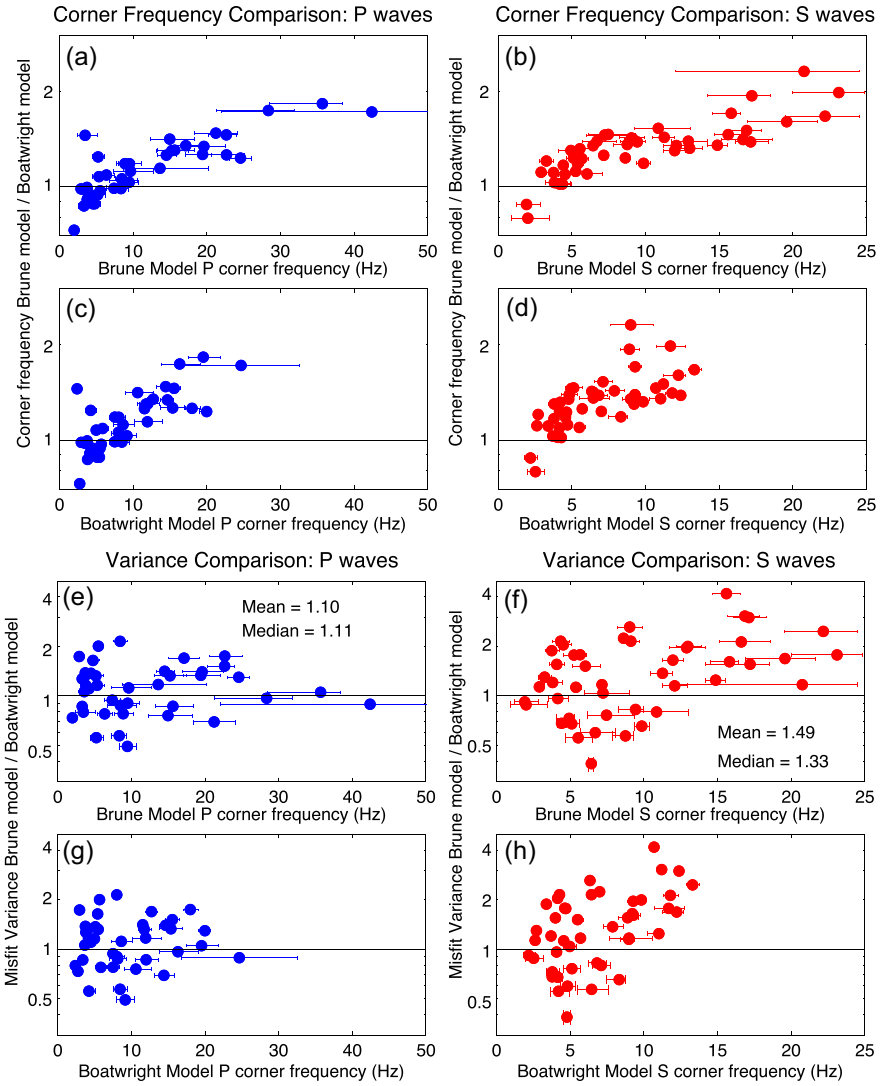

Figure 7. Comparison of fitting the stacked spectral ratios (X-correlation ≥ 0.8) from the Eketahuna sequence with both the Brune and Boatwright (sharper-cornered) source models. (a) The ratio of the *P*-wave corner frequency from the Brune model to the Boatwright model, as a function of the Brune model value. (b) The same as (a) for *S* waves. (c) and (d) show the same data as in (a) and (b) but here the abscissa values are the corner frequency values from using the Boatwright model. The two models are most consistent when the corner frequency is near the centre of the bandwidth, although there is an offset. (e) shows the ratio of the misfit variance between the Brune and Boatwright models for *P* waves, and (f) for *S* waves, both plotted against the Brune model corner frequencies. Note that for both *P* and *S*, the Brune model fits less well; both the mean and median values of the ratio are above 1. (g) and (h) are the same as (e) and (f) but with the Boatwright corner frequency on the abscissa.

a sequence have relatively few potential EGFs, and that they are, on average, smaller. Fig. S1C (Supporting Information) demonstrates the difficulty of resolving the corner frequencies for the largest earthquakes.

The sharper-cornered Boatwright-model fits the individual and stacked spectral ratios better for all sequences, and so is used for all analysis here (see Fig. S3, Supporting Information for examples of spectral fitting). A comparison of the results of the two different models of spectral shape is shown in Fig. 7. The sharper-cornered model tends to give a higher average value for the earthquakes considered here, but the relationship is strongly dependent on the relationship of the corner frequency to the bandwidth limit. The largest differences are for the poorly constrained corner frequencies near, or outside, the bandwidth limits. For corner frequencies near the low-frequency limit, the corner frequency calculated using the Boatwright model is larger than that using the Brune model; near the high-frequency limit, the reverse is true.

5.3 Uncertainty in absolute stress drops from moment and choice of source model

The results presented in Figs 4(c) and (d) include a number of key assumptions, which need to be considered before comparing the calculated stress drop values to the actual drop in stress during the earthquakes. The earthquakes are assumed to be simple, circular sources with a rupture velocity that is a fixed fraction of the shear wave velocity at the source. For example, the differences between Figs 4(b) and (d) are because of the different values of β used for the different sequences. We use the 3-D New Zealand velocity model (Eberhart-Phillips *et al.* 2010) but any variation within a sequence is ignored; this is small compared to other sources of uncertainty. The seismic moments, whether from moment tensors, or estimated from the catalogue magnitudes also contain significant uncertainties; the latter are larger, and random error could be a factor of two or three. Earthquakes in each sequence could all be

systematically high or low by a similar amount, with respect to one another. For example, there could be more overlap between the Cook Strait and Eketahuna sequences. Even a factor of four or five in seismic moment is significantly smaller than the factor of 100 variability in stress drop within one sequence, however, so this cannot explain the variation. Also, there is similar range in stress drops within the group of earthquakes with moment tensors, as there is in the earthquakes where moment is calculated from magnitude. None of these uncertainties affect the general conclusion of there being more variability within a sequence than between sequences.

The simple circular source model is a major assumption, and can lead to errors if it is inappropriate, as found by Abercrombie (2014), for example. Kaneko & Shearer (2015) show how limited azimuthal coverage can lead to uncertainties of a factor of 10, even for fairly simple sources. Any source complexity would increase this further. To minimize the effects of this assumption, we use the P to S corner frequency ratios for the best-recorded earthquakes to select a source model. We also remove the earthquakes that show clear evidence of source complexity in their STFs and spectral ratios; Fig. S1d (Supporting Information) shows an example of an excluded event. In total, we exclude only about 5 events that have well-resolved spectral ratio and STFs that are clearly complex; for comparison, almost 200 events are discarded because they are not well enough recorded, with insufficient EGFs, or too limited a frequency range to resolve either complexity or source parameters.

6 DISCUSSION AND INTERPRETATION OF STRESS DROP MEASUREMENTS

Assuming the source model and rupture velocity as discussed above, we obtain stress drops values in the range ∼1–100 MPa, with a mean value of 10 MPa (Fig. 4). The standard deviation of the $\ln(\Delta\sigma)$ values is 1.67, similar to the stress drop variability found in previous studies (Cotton *et al*. 2013). Variations in these assumptions could easily lead to a factor of 5–10 systematic increase or decrease in these values for absolute stress drop and so caution must be used in interpreting them. They are of similar magnitude to the stress drop measurements found in many previous studies using similar assumptions, elsewhere in the world, for example, Abercrombie (1995), Shearer *et al*. (2006), and Viegas *et al*. (2010).

Given the various uncertainties discussed above, we do not believe it is possible to resolve any clear systematic difference between the average properties of earthquakes in the different sequences. The variation within a sequence is much larger, and prevents any reliable distinctions between sequences with this quantity of earthquakes. If there are any systematic differences in stress drop with tectonic setting, then they are so small that much larger data sets are required to resolve them with any statistical confidence. Even in this case, there is the ambiguity as to whether any differences are caused by incorrect assumptions about the velocity and other parameters that also change with tectonic setting.

We do not see any clear trend of stress drop with source depth either within, or between sequences. We interpret our observations as being consistent with self-similar, scale-independent rupture, within the uncertainties. Any tendency for the smaller earthquakes to have lower stress drops can easily be explained by the finite bandwidth and the resulting selection bias discussed in Section 7.2.

The small-scale relative variability of earthquake stress drop within the individual sequences appears well resolved. Baltay *et al*. (2013) also concluded, after detailed analysis using multiple approaches, that there is significant variability in stress drop between earthquakes. For example, compare the spectral ratios of the two similar-sized earthquakes from the Eketahuna sequence, located only 4 km apart, in Fig. 2; further seismograms and spectra from these two earthquakes are shown in Figs S2–S7 (Supporting Information). The high correlation between the independent P- and S-wave measurements also supports this conclusion. Of course, even on this scale there could be considerable variation in attenuation, which is known to vary strongly within and near faults zones (e.g. Abercrombie 2000; Peng *et al*. 2003). The EGFs used for these two earthquakes are not the same, suggesting that these small-scale variations are accounted for. Such variability could represent either a highly heterogeneous stress field following the main shock, or variations in fault properties, including fault roughness (e.g. Candela *et al*. 2011), or geometrical complexity.

In common with many previous earthquake stress drop studies, we find that there is more variability at small magnitudes (e.g. Calderoni *et al*. 2013). This is partly, and possibly completely, a consequence of there being more small earthquakes in any data set. Alternatively, it could be a real effect consistent with the idea of increasing heterogeneity at small wavelengths, while larger earthquakes average over larger areas of the fault (Ben-Zion & Zhu 2002). The actual stress drop calculated also depends on spatial resolution and smoothing as demonstrated by both Minson *et al*. (2014) and Brown *et al*. (2015) for the great earthquake off Tohoku in 2011. Clearly, the larger earthquakes in any study will have better spatial resolution and less smoothing than the smaller ones so this is another consequence of trying to look at a relatively scale-independent process with finite bandwidth data.

7 CONCLUSIONS

We calculate stress drops for 176 earthquakes (M2.6–M6.6) from four sequences of earthquakes in New Zealand, two in the subducting Pacific plate, one in the over-riding plate and one at the subduction interface. We use the EGF approach, with strict selection criteria for EGF quality. The mean value (highly dependent on source model assumptions) for all the earthquakes is 10 MPa.

(1) Stacking over the spectral ratios for the best EGFs produces better resolved, less biased results than fitting the spectral ratios individually.

(2) There is variability of up to two orders of magnitude in stress drop within individual sequences and tectonic settings, over relatively small scale.

(3) High correlation between independent measurements of P and S waves confirm the stress drop variability.

(4) No significant systematic difference is observed between earthquakes in the upper and lower plates, or at the plate boundary.

(5) Significant uncertainties are inherent in stress drop analysis. The choice of spectral model affects the results. In particular, corner frequency estimates within 50–25 per cent of the signal frequency bandwidth limits can be significantly biased.

ACKNOWLEDGEMENTS

We are grateful to D. Trugman and C. Ruhl for their comments on an early version of this manuscript, and for constructive reviews by M. Boettcher and A. Oth. The seismic phase data, waveform data and moment tensor data used in this study were accessed through New

Zealand GeoNet (http://www.geonet.org.nz; last accessed: 2016 May 26). This research was sponsored by the National Science Foundation (USA), award no. 1113593, and supported by public research funding from the Government of New Zealand. Maps were drawn using the Generic Mapping Tools (Wessel & Smith 1998), and some analysis was carried out using ObsPy (Beyreuther *et al*. 2010).

REFERENCES

Abercrombie, R.E., 1995. Earthquake source scaling relationships from −1 to 5 M_L using seismograms recorded at 2.5 km depth, *J. geophys. Res.,* **100,** 24 015–24 036.

Abercrombie, R.E., 2000. Crustal attenuation and site effects at Parkfield, California, *J. geophys. Res.,* **105**(B3), 6277–6286.

Abercrombie, R.E., 2013. Comparison of direct and coda wave stress drop measurements for the Wells, Nevada, earthquake sequence, *J. geophys. Res.,* **118,** 1458–1470.

Abercrombie, R.E., 2014. Stress drops of repeating earthquakes on the San Andreas fault at Parkfield, *Geophys. Res. Lett.,* **41,** 8784–8791.

Abercrombie, R.E., 2015. Investigating uncertainties in Empirical Green's function analysis earthquake source parameters, *J. geophys. Res.,* **120**(6), 4263–4377.

Abercrombie, R.E. & Rice, J.R., 2005. Small earthquake scaling revisited: can it constrain slip weakening?, *Geophys. J. Int.,* **162,** 406–424.

Allmann, B.B. & Shearer, P.M., 2009. Global variations of stress drop for moderate to large earthquakes, *J. geophys. Res.,* **114**, doi:10.1029/2009JB005821.

Allmann, B.P. & Shearer, P.M., 2007. Spatial and temporal stress drop variations in small earthquakes near Parkfield, California, *J. geophys. Res.,* **112**(B4), B04305, doi:10.1029/2006JB004395.

Baltay, A.S., Hanks, T.C. & Beroza, G.C., 2013. Stable stress-drop measurements and their variability: implications for ground-motion prediction, *Bull. seism. Soc. Am.,* **103,** 211–222.

Ben-Zion, Y. & Zhu, L., 2002. Potency-magnitude scaling relations for Southern California earthquakes with $1.0 < M_L < 7.0$, *Geophys. J. Int.,* **148,** F1–F5.

Beyreuther, M., Barsch, R., Krischer, L., Megies, T., Behr, Y. & Wassermann, J., 2010. ObsPy: a python toolbox for seismology, *Seismol. Res. Lett.,* **81**(3), 530–533.

Boatwright, J., 1980. A spectral theory for circular seismic sources: simple estimates of source dimension, dynamic stress drop, and radiated seismic energy, *Bull. seism. Soc. Am.,* **70,** 1–28.

Brown, L., Wang, K. & Sun, T., 2015. Static stress drop in the M_w 9 Tohoku-oki earthquake: heterogeneous distribution and low average value, *Geophys. Res. Lett.,* **42**, doi:10.1002/2015GL066361.

Brune, J., 1970. Tectonic stress and the spectra of seismic shear waves from earthquakes, *J. geophys. Res.,* **75,** 4997–5009.

Calderoni, G., Rovelli, A. & Singh, S.K., 2013. Stress drop and source scaling of the 2009 April L'Aquila earthquakes, *Geophys. J. Int.,* **192**(1), 260–274.

Candela, T., Renard, F., Bouchon, M., Schmittbuhl, J. & Brodsky, E.E., 2011. Stress drop during earthquakes: effect of fault roughness scaling, *Bull. seism. Soc. Am.,* **101,** 2369–2387.

Chen, X. & Shearer, P.M., 2011. Comprehensive analysis of earthquake source spectra and swarms in the Salton Trough, California, *J. geophys. Res.,* **116**, doi:10.1029/2011JB008263.

Choy, G.L., McGarr, A., Kirby, S.H. & Boatwright, J., 2006. An overview of the global variability in radiated energy and apparent stress, in *Earthquakes: Radiated Energy and the Physics of Faulting*, AGU Geophysical Monograph Series, pp. 43–57, eds Abercrombie, R., McGarr, A., Di Toro, G. & Kanamori, H.

Cotton, F., Archuleta, R. & Causse, M., 2013. What is the sigma of the stress drop?, *Seismol. Res. Lett.,* **84,** 42–48.

Davy, B., Hornle, K. & Werner, R., 2008. Hikurangi Plateau: crustal structure, rifted formation, and Godwana subduction history, *Geochem. Geophys. Geosyst.,* **9**, doi:10.1029/2007GC001855.

Del Gaudio, S., Causse, M. & Festa, G., 2015. Broad-band strong motion simulations coupling k-square kinematic source models with empirical Green's functions: the 2009 L'Aquila earthquake, *Geophys. J. Int.,* **203,** 720–736.

Eberhart-Phillips, D., Reyners, M.E., Bannister, S.C., Chadwick, M.P. & Ellis, S.M., 2010. Establishing a versatile 3-D seismic velocity model for New Zealand, *Seismol. Res. Lett.,* **81**(6), 992–1000.

Eshelby, J.D., 1957. The determination of the elastic field of an ellipsoidal inclusion and related problems, *Proc. R. Soc. Lond., A,* **241**, 376–396.

Felzer, K.R., Becker, T.W., Abercrombie, R.E., Ekström, G. & Rice, J.R., 2002. Triggering of the 1999 M_w 7.1 Hector Mine earthquake by aftershocks of the 1992 M_w 7.3 Landers earthquake, *J. geophys. Res.,* **107,** 2190, doi:10.1029/2001JB000911.

Field, E.H. *et al.*, 2015. Long-term time-dependent probabilities for the Third Uniform California Earthquake Rupture Forecast (UCERF3), *Bull. seism. Soc. Am.,* **105,** 511–543.

Fry, B. & Gerstenberger, M.C., 2011. Large apparent stresses from the Canterbury earthquakes of 2010 and 2011, *Seismol. Res. Lett.,* **82**(6), 833–838.

Gale, N., Gledhill, K., Chadwick, M. & Wallace, L., 2015. The Hikurangi margin continuous GNSS and seismograph network of New Zealand, *Seismol. Res. Lett.,* **86**(1), doi:10.1785/0220130181.

Hamling, I.J., D'Anastasio, E., Wallace, L.M., Ellis, S.M., Motagh, M., Samsonov, S., Palmer, N.G. & Hreinsdottir, S., 2014. Crustal deformation and stress transfer during a propagating earthquake sequence: the 2013 Cook Strait sequence, Central New Zealand, *J. geophys. Res.,* **119**(7), 6080–6092.

Hanks, T.C. & Kanamori, H., 1979. A moment magnitude scale, *J. geophys. Res.,* **84**(5), 2348–2350.

Hardebeck, J.L. & Aron, A., 2009. Earthquake stress drops and inferred fault strength on the Hayward Fault, East San Francisco Bay, California, *Bull. seism. Soc. Am.,* **99,** 1801–1814.

Hartung, J., Knapp, G. & Sinha, B.K., 2008. *Statistical Meta-Analysis With Applications*, John Wiley & Sons.

Holden, C., 2011. Kinematic source model of the 22 February 2011 M_w 6.2 Christchurch earthquake using strong motion data, *Seismol. Res. Lett.,* **82**(6), 783–788.

Holden, C., Kaiser, A., Van Dissen, R. & Jury, R., 2013. Sources, ground motion and structural response characteristics in Wellington of the 2013 Cook Strait earthquakes, *Bull. N. Z. Soc. Earthq. Eng.,* **46**(4), 188–195.

Ide, S., Beroza, G.C., Prejean, S.G. & Ellsworth, W.L., 2003. Apparent break in earthquake scaling due to path and site effects on deep borehole recordings, *J. geophys. Res.,* **108,** 2271, doi:10.1029/2001JB001617.

Kanamori, H. & Anderson, D.L., 1975. Theoretical basis of some empirical relations in seismology, *Bull. seism. Soc. Am.,* **65**(5), 1073–1095.

Kane, D.L., Kilb, D.L. & Vernon, F.L., 2013. Selecting Empirical Green's functions in regions of fault complexity: a study of data from the San Jacinto Fault Zone, Southern California, *Bull. seism. Soc. Am.,* **103**(2A), doi:10.1785/0120120189.

Kaneko, Y. & Shearer, P.M., 2014. Seismic source spectra and estimated stress drop from cohesive-zone models of circular subshear rupture, *Geophys. J. Int.,* **197,** 1002–1015.

Kaneko, Y. & Shearer, P.M., 2015. Variability of seismic source spectra, estimated stress drop and radiated energy, derived from cohesive-zone models of symmetrical and asymmetrical circular and elliptical ruptures, *J. geophys. Res.,* **120**(2), 1053–1079.

Ko, Y.-T., Kuo, B.-Y. & Hung, S.-H., 2012. Robust determination of earthquake source parameters and mantle attenuation, *J. geophys. Res.,* **117,** B04304, doi:10.1029/2011JB008759.

Kwiatek, G., Bulut, F., Bohnhoff, M. & Dresen, G., 2014. High-resolution analysis of seismicity induced at Berlín geothermal field, El Salvador, *Geothermics,* **52,** 98–111.

Kwiatek, G., Plenkers, K. & Dresen, G., 2011. Source parameters of picoseismicity recorded at Mponeng deep gold mine, South Africa: implications for scaling relations, *Bull. seism. Soc. Am.,* **101,** 2592–2608.

Madariaga, R., 1976. Dynamics of an expanding circular crack, *Bull. seism. Soc. Am.,* **66,** 639–666.

Minson, S.E. *et al.*, 2014. A Bayesian approach to finite fault earthquake modeling II: Application to the Great 2011 Tohoku-Oki earthquake, *Geophys. J. Int.,* **198**(2), 922–940.
Mori, J. & Frankel, A., 1990. Source parameters for small events associated with the 1986 North Palm-Springs, California, earthquake determined using empirical Green-functions, *Bull. seism. Soc. Am.,* **80**, 278–295.
Nakano, K., Matsushima, S. & Kawase, H., 2015. Statistical properties of strong ground motions from the generalized spectral inversion of data observed by K-NET, KiK-net and the JMA Shindokei Network in Japan, *Seismol. Soc. Am.,* **105,** 2662–2680.
Oth, A., 2013. On the characteristics of earthquake stress release variations in Japan, *Earth planet. Sci. Lett.,* **377–378,** 132–141.
Oth, A. & Kaiser, A.E., 2014. Stress release and source scaling of the 2010–2011 Canterbury, New Zealand, earthquake sequence from spectral inversion of ground motion data, *Pure appl. Geophys.*, doi:10.1007/s00024-013-0751-1.
Oth, A., Bindi, D., Parolai, S. & Di Giacomo, D., 2011. Spectral analysis of K-NET and KiK-net data in Japan, Part II: On attenuation characteristics, source spectra, and site response of borehole and surface stations, *Bull. seism. Soc. Am.,* **101,** 667–687.
Pacor, F. *et al.*, 2016. Spectral models for ground motion prediction in the L'Aquila region (Central Italy): evidence for stress drop dependence on magnitude and depth, *Geophys. J. Int.,* **204,** 716–737.
Park, J., Lindberg, C.R. & Vernon, F.L., III, 1987. Multitaper spectral analysis of high-frequency seismograms, *J. geophys. Res.,* **92,** 12675–12684.
Peng, Z., Ben-Zion, Y., Michael, A.J. & Zhu, L., 2003. Quantitative analysis of seismic trapped waves in the rupture zone of the 1992 Landers, California earthquake: evidence for a shallow trapping structure, *Geophys. J. Int.,* **155,** 1021–1041.
Prieto, G.A., Parker, R.L., Vernon, F.L., Shearer, P.M. & Thomson, D.J., 2006. Uncertainties in earthquake source spectrum estimation using empirical Green functions, in *Earthquakes: Radiated Energy and the Physics of Faulting*, AGU Geophysical Monograph Series, Vol. 170, doi:10.1029/170GM08.
Prieto, G.A., Parker, R.L. & Vernon, I.F.L., 2009. A Fortran 90 library for multitaper spectrum analysis, *Comput. Geosci.,* **35,** 1701–1710.
Reyners, M.E. & Bannister, S.C., 2007. Earthquakes triggered by slow slip at the plate interface in the Hikurangi subduction zone, New Zealand, *Geophys. Res. Lett.,* **34**(14), L14305, doi:10.1029/2007GL030511.
Ristau, J., 2009. Comparison of magnitude estimates for New Zealand earthquakes: moment magnitude, local magnitude, and teleseismic body-wave magnitude, *Bull. seism. Soc. Am.,* **99,** 1841–1852.
Ristau, J., 2013. Update of regional moment tensor analysis for earthquakes in New Zealand and adjacent offshore regions, *Bull. seism. Soc. Am.,* **103,** 2520–2533.
Ruhl, C., Abercrombie, R.E. & Smith, K., 2016. Variability of source parameter estimates for the 2008 Mogul earthquake swarm near Reno, NV using EGF-derived spectral ratios, *Seism. Res. Lett.,* **87**(2B), 556.
Shearer, P.M., Prieto, G.A. & Hauksson, E., 2006. Comprehensive analysis of earthquake source spectra in southern California, *J. geophys. Res.,* **111,** B06303, doi:10.1029/2005JB003979.
Sibson, R.H., 1974. Frictional constraints on thrust, wrench and normal faults, *Nature,* **249,** 542–544.
Uchida, N., Matsuzawa, T., Ellsworth, W.L., Imanishi, K., Shimamura, K. & Hasegawa, A., 2012. Source parameters of microearthquakes on an interplate asperity off Kamaishi, NE Japan over two earthquake cycles, *Geophys. J. Int.,* **189,** 999–1014.
Uchide, T. & Imanishi, K., 2016. Small earthquakes deviate from the omega-square model as revealed by multiple spectral ratio analysis, *Bull. seism. Soc. Am.,* **106,** 1357–1363.
Viegas, G.M., Abercrombie, R.E. & Kim, W.-Y., 2010. The 2002 M5 Au Sable Forks, NY, earthquake sequence: source scaling relationships and energy budget, *J. geophys. Res.,* **115,** B07310, doi:10.1029/2009JB006799.
Waldhauser, F. & Ellsworth, W.L., 2000. A double-difference earthquake location algorithm: method and application to the northern Hayward fault, California, *Bull. seism. Soc. Am.,* **90,** 1353–1368.
Wallace, L.M., Bartlow, N., Hamling, I. & Fry, B., 2014. Quake clamps down on slow slip, *Geophys. Res. Lett.,* **41,** 8840–8846.
Wessel, P. & Smith, W.H.F., 1998. New, improved version of the Generic Mapping Tools released, *EOS, Trans. Am. geophys. Un.,* **79**(47), 579–579.
Williams, C.A., Eberhart-Phillips, D., Bannister, S., Barker, D.H.N., Henrys, S., Reyners, M. & Sutherland, R., 2013. Revised interface geometry for the Hikurangi subduction zone, New Zealand, *Seismol. Res. Lett.,* **84**(6), doi:10.1785/0220130035.

SUPPORTING INFORMATION

Additional Supporting Information may be found in the online version of this paper:

Figure S1. Further examples of earthquakes as shown in Fig. 2 of the main text. (a) M4.1 (ID496) event at Eketahuna, (b) M3.3 (ID236) event at Eketahuna, (c) the three largest Cook Strait earthquakes: M6.7 (ID923), M6.2 (ID1088) and M6.0 (ID1120), only *S*-wave ratios met the quality criteria and (d) M3.4 (ID590) event at Eketahuna showing evidence of complexity in both the *P* and *S* waves, and in both the spectral ratios and the source time functions. The earthquakes ID1120 (S1c) and ID590 (S1d) were excluded from subsequent analysis because of the obvious complexity and consequent poor fit making the simple source model inappropriate. The corner frequency of earthquake ID1088 (S1c) may also be overestimated.
Figure S2. Example of fitting individual spectral ratios. Earthquake ID327 (M3.8), with earthquake ID23 (M2.3) as EGF, at station HOWZ on the vertical component, *P* waves. (a) The main event (black) and EGF (red) seismograms, the thick lines are the time window used to calculate spectra. Also given are the cross-correlation values between these time windows for the raw seismograms, and for the filtered ones (see the text), together with the low-pass limit of the filter. (b) Displacement spectra for the main and EGF events, and preceding noise windows. No instrument correction. (c) The relative source time function calculated in the complex spectral division. It is not filtered, so includes noise, and is used here only to indicate whether the EGF assumption works in phase as well as amplitude. (d) Fit to the spectral ratio within the frequency range above the noise level, using the sharper-cornered Boatwright model. The rainbow colours are the results of a grid search around the best-fitting corner frequency. The absolute variance, relative to the long-period amplitude of the ratio, is given. The relative variance in fit, and long-period amplitude level, and small event corner frequency are shown in (e) and (f). The 'fit_slope' and 'fc error' shown in (e) are the quality criteria fit_amp_ratio and fc1_err referred to in the text. (g)–(i) show the fits using the original Brune model, following (d)–(f). The variance in (g) is directly comparable with that in (d).
Figure S3. Example of fitting individual spectral ratios. Earthquake ID327 (M3.8), with earthquake ID23 (M2.3) as EGF, at station HOWZ on the north component, *S* waves. See Fig. S2 (Supporting Information) for detailed description.
Figure S4. Example of fitting individual spectral ratios. Earthquake ID327 (M3.8), with earthquake ID557 (M2.5) as EGF, at station TMWZ on the vertical component, *P* waves. See Fig. S2 (Supporting Information) for detailed description.
Figure S5. Example of fitting individual spectral ratios. Earthquake ID327 (M3.8), with earthquake ID557 (M2.5) as EGF, at station TMWZ on the north component, *S* waves. See Fig. S2 (Supporting Information) for detailed description.
Figure S6. Example of fitting individual spectral ratios. Earthquake ID468 (M3.8), with earthquake ID495 (M2.3) as EGF, at station

TMWZ on the vertical component, *P* waves. See Fig. S2 (Supporting Information) for detailed description.

Figure S7. Example of fitting individual spectral ratios. Earthquake ID468 (M3.8), with earthquake ID324 (M2.4) as EGF, at station TMWZ on the east component, *S* waves. See Fig. S2 (Supporting Information) for detailed description.

Figure S8. Stress drop results for the Eketahuna sequence from fitting the stacked spectral ratios, as a function of cross-correlation and assumed source model. The calculated stress drops are plotted at the minimum cross-correlation (X-correlation) included in the stack, with a random offset to make plotting clearer. The earthquakes shown in Fig. 2 and Fig. S1 (Supporting Information), for which stress drop estimates can be calculated, are labelled. Note that the stress drops for ev327 are consistently higher than for ev468. Also, the values for ev590 are anomalously low; this is not surprising as this earthquake has a complex source and so the assumed source models are inappropriate.

Table S1. Hypocentral information, and corner frequency values of the earthquakes analysed. These data are presented as four comma-delimited text files for easy reading into various software packages. When there is a finite number of ratios included in a stack, but the source parameters are all zero, then it indicates that the fits were judged unreliable (see, e.g. Figs S1c and d, Supporting Information).
Table S1a_Hypo_param_EKE_GJI.txt
Table S1b_Hypo_param_UH_GJI.txt
Table S1c_Hypo_param_POG_GJI.txt
Table S1d_Hypo_param_CKS_GJI.txt
(http://gji.oxfordjournals.org/lookup/suppl/doi:10.1093/gji/ggw393/-/DC1).

Please note: Oxford University Press is not responsible for the content or functionality of any supporting materials supplied by the authors. Any queries (other than missing material) should be directed to the corresponding author for the paper.